

Non-reciprocal and artificial Λ-type systems in waveguide QED with parametrically modulated superconducting qubits

Bing-Jie Chen(陈炳杰), Li Li(李力), Rui-Yang Gong(龚锐洋), Silu Zhao(赵思路), Shi Xiao(肖师), Xiaohui Song(宋小会), Zhongcheng Xiang(相忠诚), and Dongning Zheng(郑东宁)

Citation: Chin. Phys. B, 2026, 35 (**6**): 064204. DOI: 10.1088/1674-1056/ae4f71
http://cpb.iphy.ac.cn; http://iopscience.iop.org/cpb

What follows is a list of articles you may be interested in

Multi-frequency non-reciprocal optical directional amplifier realized with non-Hermitian resonator arrays

Jin-Xiang Xue(薛金香), Chuan-Xun Du(杜传勋), Cheng-Chao Liu(刘成超), Liu Yang(杨柳), and Yong-Long Wang(王永龙)
Chin. Phys. B, 2026, 35 (**2**): 024207. DOI: 10.1088/1674-1056/adf69d

Controllable phase-dependent optical switch in an atom-cavity system

Xu-Yang Li(李旭阳), Yuan-Feng Lu(陆元峰), Ya-Jie Wu(吴亚杰), Ning Li(荔宁), and Miao-Di Guo(郭苗迪)
Chin. Phys. B, 2026, 35 (**2**): 024205. DOI: 10.1088/1674-1056/adfc40

Room-temperature exciton-polariton condensation in pressed perovskite microcavities

Tianyin Zhu(朱天寅), Zelei Chen(陈泽磊), Xiaoyu Wang(王小宇), Zhongmin Huang(黄钟民), Haibin Zhao(赵海斌), and Jun Wang(王俊)
Chin. Phys. B, 2025, 34 (**9**): 094202. DOI: 10.1088/1674-1056/addce6

Nonreciprocal two-photon transmission and statistics in a chiral waveguide QED system

Lei Wang(王磊), Zhen Yi(伊珍), Li-Hui Sun(孙利辉), and Wen-Ju Gu(谷文举)
Chin. Phys. B, 2022, 31 (**5**): 054206. DOI: 10.1088/1674-1056/ac3ecc

Realization of adiabatic and diabatic CZ gates in superconducting qubits coupled with a tunable coupler

Huikai Xu(徐晖凯), Weiyang Liu(刘伟洋), Zhiyuan Li(李志远), Jiaxiu Han(韩佳秀), Jingning Zhang(张静宁), Kehuan Linghu(令狐克寰), Yongchao Li(李永超), Mo Chen(陈墨), Zhen Yang(杨真), Junhua Wang(王骏华), Teng Ma(马腾), Guangming Xue(薛光明), Yirong Jin(金贻荣), and Haifeng Yu(于海峰)
Chin. Phys. B, 2021, 30 (**4**): 044212. DOI: 10.1088/1674-1056/abf03a

---

RAPID COMMUNICATION

Non-reciprocal and artificial Λ-type systems in waveguide QED with parametrically modulated superconducting qubits

Bing-Jie Chen(陈炳杰)[1,2], Li Li(李力)[1,2], Rui-Yang Gong(龚锐洋)[3], Silu Zhao(赵思路)[1,2], Shi Xiao(肖师)[1,2,4], Xiaohui Song(宋小会)[1,2,5], Zhongcheng Xiang(相忠诚)[1,2,5], and Dongning Zheng(郑东宁)[1,2,5,†]

[1] *Beijing National Laboratory for Condensed Matter Physics, Institute of Physics, Chinese Academy of Sciences, Beijing* 100190, *China*
[2] *University of Chinese Academy of Sciences, Beijing* 100049, *China*
[3] *School of Physics, Sun Yat-sen University, Guangzhou* 510275, *China*
[4] *Key Laboratory of Low-Dimensional Quantum Structures and Quantum Control of Ministry of Education, Department of Physics and Synergetic Innovation Center for Quantum Effects and Applications, Hunan Normal University, Changsha* 410081, *China*
[5] *Hefei National Laboratory, Hefei* 230088, *China*

(Received 20 January 2026; revised manuscript received 25 February 2026; accepted manuscript online 10 March 2026)

We present a non-local quantum system based on a waveguide QED architecture, comprising two spatially separated and largely detuned superconducting transmon qubits. By applying parametric frequency modulation to one of the qubits, we establish a tunable coherent channel between the two far-detuned qubits, thereby forming an Λ-type three-level system. We demonstrate that tuning the modulation amplitude enables the observation of spectral evolution from electromagnetically induced transparency (EIT) to Autler–Townes splitting (ATS). Furthermore, by exploiting the interplay between the non-local waveguide phase and system dissipation, the system achieves significant non-reciprocal microwave transmission and direction-selective photon emission. The scheme operates without external magnetic fields, offering an efficient pathway for realizing on-chip integrated quantum routers and isolators.

Keywords: waveguide QED, superconducting qubits, parametric modulation

PACS: 42.50.Pq, 42.50.Gy, 03.65.Yz, 03.67.Lx

DOI: 10.1088/1674-1056/ae4f71 **CSTR:** 32038.14.CPB.ae4f71

1. Introduction

Over the past two decades, circuit quantum electrodynamics (circuit QED) based on superconducting circuits has emerged as a leading platform for exploring quantum optics and realizing quantum information processing.[1–6] Enabled by the strong coupling capability between artificial atoms[7] and microwave photons, this field has witnessed significant progress in single-photon generation,[8,9] quantum logic gates,[10,11] the preparation of multiparticle entangled states,[12] and microwave photon detection.[13] In particular, waveguide QED architectures based on one-dimensional open transmission lines offer an ideal hardware foundation for building large-scale quantum networks and distributed quantum computing.[14–18] The applied microwave modulation induces an effective magnetic flux bias that breaks the system's reciprocity, offering an efficient pathway for realizing on-chip integrated quantum routers and isolators without external magnetic fields.

In quantum network nodes, three-level systems capable of coherently manipulating photon transmission are important. Electromagnetically induced transparency (EIT) based on Λ-type levels serves not only as a core mechanism for realizing quantum memory[19,20] but also as the basis for building single-photon transistors and switches.[16,21,22] However, realizing this goal in superconducting circuits faces an inherent obstacle: common superconducting transmon qubits typically exhibit a ladder-type energy level structure and lack the metastable states required for Λ-type systems.[23–26] To overcome this limitation, researchers have proposed various schemes, such as introducing auxiliary resonator modes, utilizing specific energy level structures near flux sweet spots, or constructing artificial molecules based on multi-qubit coupling.[27,28] In addition, parametric modulation serves as an effective strategy to engineer such systems. By applying parametric frequency modulation to a single qubit, forbidden sideband transitions can be activated to construct an equivalent Λ-type system without the need for complex circuit designs.[29,30] Similarly, parametric drives have been demonstrated to facilitate coherent exchange between symmetric and antisymmetric states in coupled qubit pairs, thereby mimicking Λ-type transitions.[31]

While these works have successfully established the basis for energy level engineering, extending such schemes to the non-reciprocal regime offers significant potential. Achieving direction-dependent transmission is essential for enabling

[†]Corresponding author. E-mail: dzheng@iphy.ac.cn

© 2026 Chinese Physical Society and IOP Publishing Ltd. All rights, including for text and data mining, AI training, and similar technologies, are reserved.

advanced functionalities like signal isolation and directional routing in quantum networks. To break Lorentz reciprocity, it is typically necessary to introduce magneto-optical effects, time-varying modulation, or chiral coupling.[32–35] In recent years, achieving non-reciprocity via parametric modulation has attracted significant attention. For instance, modulation techniques have been successfully applied to quantum beam splitters based on parity–time (PT) symmetry to realize non-reciprocal control of high-order quantum correlations ($g^{(2)}$).[36] Building upon these foundations, realizing efficient, tunable, and structurally simple non-reciprocal devices at the single-photon level represents a highly desirable goal for scalable waveguide QED architectures.[37,38] Alongside these developments, actively modifying atomic decay rates and directional radiation behaviors through tunable environments is also attracting broad interest across various macroscopic QED platforms.[39]

Inspired by giant atom physics and multi-point interference effects,[40–44] we propose a novel waveguide QED system combining parametric modulation techniques with non-local waveguide coupling. Distinct from previous approaches relying on local single-qubit modulation[39] or PT-symmetric configurations,[36] we utilize two spatially separated and largely detuned transmon qubits, applying parametric modulation to only one of them. In this architecture, parametric modulation compensates for the energy detuning between qubits to establish a coherent channel, constructing the Λ system. More critically, we exploit the non-local phase factor $\varphi_{\rm w}$ introduced by waveguide propagation as an additional degree of freedom. Through its interplay with system dissipation, we break the time-reversal symmetry of the system,[45,46] achieving a maximum non-reciprocity parameter of 0.9999.

The remainder of this paper is organized as follows. Section 2 constructs the non-local two-qubit model with parametric modulation and derives the effective Hamiltonian. Section 3 analyzes the steady-state spectral properties, demonstrating the controllable evolution from EIT to ATS.[47] Section 4 explores the mechanism of non-reciprocal transmission induced by waveguide phase delay. Section 5 presents the dynamical characteristics of the system as a tunable directional quantum emitter.[48] Finally, we conclude in Section 6. Our scheme requires no external magnetic fields and provides a new approach for realizing quantum routing and isolation via parametric modulation using standard superconducting fabrication processes.

2. Model and effective Hamiltonian

Figure 1(a) illustrates the architecture of the waveguide QED system proposed in this study. The system comprises two spatially separated superconducting transmon qubits collectively coupled to the continuum of a one-dimensional open waveguide. In this architecture, the transition frequency ω_1 of qubit 1 remains fixed, serving as a static reference. In contrast, the transition frequency $\omega_2(t)$ of qubit 2 undergoes periodic parametric modulation, acting as a control knob to actively tune the coherent coupling of the system. The long-range interaction between the qubits is mediated by microwave photons propagating along the waveguide. This non-local character introduces a propagation phase factor defined as $\varphi_{\rm w} = k|x_1 - x_2|$, where k denotes the wavenumber of the propagating microwave mode.

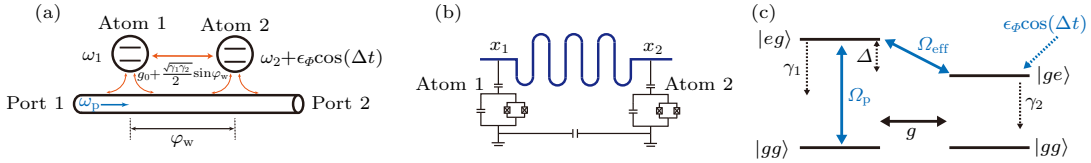


Fig. 1. Schematic of the system architecture and energy levels. (a) Two spatially separated transmon qubits coupled to a 1D waveguide, with their interaction modulated by the propagation phase $\varphi_{\rm w}$. (b) Diagram of the interaction between the probe field and the qubits, illustrating the definition of the local phase φ_j. (c) The effective Λ-type three-level system model in the rotating frame.

In the laboratory frame, the total system Hamiltonian ($\hbar = 1$), which encompasses the qubit eigenenergies, external probe drives, and non-local qubit–qubit interactions, is expressed as[49]

$$\begin{aligned} H_{\rm lab} =\ & \omega_1 a_1^\dagger a_1 + [\omega_2 + \epsilon_\Phi \cos(\Delta t)] a_2^\dagger a_2 \\ & + \alpha_0 a_1^\dagger a_1^\dagger a_1 a_1 + \alpha_0 a_2^\dagger a_2^\dagger a_2 a_2 \\ & + \left(g_0 + \frac{\sqrt{\gamma_1\gamma_2}}{2}\sin\varphi_{\rm w}\right)(a_1^\dagger a_2 + a_1 a_2^\dagger) \\ & - {\rm i}\sum_{j=1,2}\sqrt{\frac{\gamma_j}{2}}[(\alpha\, {\rm e}^{{\rm i}(\omega_{\rm p}t+\varphi_j)} a_j^\dagger - \alpha^*\, {\rm e}^{-{\rm i}(\omega_{\rm p}t+\varphi_j)} a_j]. \end{aligned} \tag{1}$$

Here, $a_j^\dagger$ (a_j) denotes the creation (annihilation) operator for the j-th qubit. The first line of Eq. (1) describes the uncoupled eigenenergies of the system, where ϵ_Φ and Δ represent the modulation amplitude and frequency of qubit 2, respectively. The second line represents the anharmonic terms of the qubits, where α_0 denotes the anharmonicity. We assume the anharmonicities of the two qubits are identical, which can be experimentally realized by controlling the capacitance of the transmon qubits. The third line explicitly provides the non-local interaction term (along with the dissipation terms), where γ_j represents the radiative decay rate of the j-th qubit into the waveguide. This interaction consists of the dissi-

pative coupling mediated by the waveguide (dependent on $\sin\varphi_w$) and the direct capacitive coupling g_0. To facilitate the subsequent discussion, we define the total effective coupling strength as $g = g_0 + \frac{\sqrt{\gamma_1\gamma_2}}{2}\sin\varphi_w$. In our experimental configuration, the system operates in the large-detuning regime ($|\omega_1 - \omega_2| \gg g, \gamma$). Consequently, the natural exchange interaction between qubits is highly suppressed by the energy difference in the absence of modulation. The coherent channel between qubits can be controllably activated only by finely tuning the modulation frequency Δ of qubit 2 to compensate for this energy detuning. The fourth line describes the coupling between the qubits and a probe field with frequency ω_p, where α denotes the complex amplitude of the incident microwave drive. Specifically, φ_j denotes the local phase of the probe signal arriving at the j-th qubit located at x_j, as schematically shown in Fig. 1(b)). By setting the reference phase $\varphi_1 = 0$, the phase at qubit 2 is naturally given by $\varphi_2 = \varphi_w$.

To treat the explicitly time-dependent Hamiltonian, we transform the system into a rotating frame defined by the unitary operator $U(t) = \exp[-i\omega_p t a_1^\dagger a_1 - i(\omega_p - \Delta - \frac{\epsilon_\Phi}{\Delta}\sin\Delta t)a_2^\dagger a_2]$. By applying the Jacobi–Anger expansion and neglecting fast-oscillating terms under the rotating-wave approximation (RWA), we derive the time-independent effective Hamiltonian under the resonance condition $\Delta = \omega_1 - \omega_2$ (see Appendix A for details). This effective Hamiltonian corresponds to an equivalent Λ-type three-level system, as depicted in Fig. 1(c):

$$\begin{aligned} H_{\rm eff} &= \Delta_p a_1^\dagger a_1 + \Delta_p a_2^\dagger a_2 + \alpha_0 a_1^\dagger a_1^\dagger a_1 a_1 + \alpha_0 a_2^\dagger a_2^\dagger a_2 a_2 \\ &\quad + \Omega_{\rm eff}(a_1^\dagger a_2 + a_1 a_2^\dagger) \\ &\quad - i\sum_{j=1,2}\sqrt{\frac{\gamma_j}{2}}\left(\alpha_j e^{i\varphi_j} a_j^\dagger - \text{H.c.}\right), \end{aligned} \tag{2}$$

where $\Delta_p = \omega_1 - \omega_p$ denotes the probe detuning, and $\alpha_1 = \alpha, \alpha_2 = \alpha J_1(\epsilon_\Phi/\Delta)$ correspond to the effective driving strengths of the incident microwave on the respective qubits. Notably, the effective coupling strength $\Omega_{\rm eff}$, induced by the parametric modulation of qubit 2, is renormalized as

$$\Omega_{\rm eff} = \left(g_0 + \frac{\sqrt{\gamma_1\gamma_2}}{2}\sin\varphi_w\right) J_1\left(\frac{\epsilon_\Phi}{\Delta}\right). \tag{3}$$

This expression indicates that the effective coupling strength is directly proportional to the first-order Bessel function $J_1(\epsilon_\Phi/\Delta)$. Therefore, by adjusting the modulation amplitude ϵ_Φ of qubit 2, we can perform switching of the coherent channel between the two spatially separated qubits, without perturbing the stability of qubit 1, which serves as the probe port.

In the subsequent sections, we investigate the system's spectral and dynamical properties based on this effective model. To optimally illustrate the distinct physical mechanisms — ranging from interference-induced transparency to chiral photon emission — we adopt specific parameter sets for different regimes. These parameter choices, along with their physical motivations, are summarized in Table 1.

Table 1. Summary of system parameters used in numerical simulations. The parameter sets are selected to optimize the visibility of distinct physical mechanisms.

Figure	Phenomenon	Decay rates (γ_1, γ_2) (MHz)	Physical motivation/regime
Fig. 2	EIT/ATS transition	20, 10	Maximize linewidth contrast to resolve modes
Fig. 3	Non-reciprocal Trans.	20, 10	Enhance interference for high isolation contrast
Fig. 4	Directional emission	10, 10	Demonstrate chirality from modulation

*Note: Unless otherwise stated, other common system parameters are fixed at $\omega_{1,2}/2\pi \approx 6, 5.8$ GHz, $g_0/2\pi = 20$ MHz, and $v \approx 1.2\times10^8$ m/s.

3. Steady-state transmission and spectroscopy

To investigate the optical response of the system to the probe field Ω_p, we employ the Lindblad master equation to describe its open quantum dynamics. Unlike traditional cavity QED systems, the waveguide-mediated interaction not only renormalizes the Hamiltonian but also introduces non-local collective dissipation. In the rotating frame, the master equation takes the form

$$\dot\rho = -i[H_{\rm eff}, \rho] + \sum_{j=1,2}\mathcal{L}_j[\rho] + \mathcal{L}_{\rm coll}[\rho], \tag{4}$$

where $\mathcal{L}_j = \gamma_j\mathcal{D}[a_j] + 2\gamma_{\phi,j}\mathcal{D}[a_j^\dagger a_j]$ accounts for the individual relaxation γ_j and pure dephasing $\gamma_{\phi,j}$ of the j-th qubit. Here, the Lindblad superoperator is defined as $\mathcal{D}[O]\rho = O\rho O^\dagger - \frac{1}{2}\{O^\dagger O, \rho\}$. The collective dissipation term $\mathcal{L}_{\rm coll}$ describes the interference effects arising from the two qubits coupling to the common waveguide bath:

$$\begin{aligned} \mathcal{L}_{\rm coll}[\rho] &= \sqrt{\gamma_1\gamma_2}\cos\varphi_w J_1\left(\frac{\epsilon_\Phi}{\Delta}\right) \\ &\quad \times \left(a_1\rho a_2^\dagger - \frac{1}{2}\{a_1^\dagger a_2, \rho\} + \text{H.c.}\right). \end{aligned} \tag{5}$$

The presence of this term, which depends on $\cos\varphi_w$, implies that the radiation fields of the two qubits can undergo constructive or destructive interference. This interference is the key mechanism for realizing non-reciprocal transmission and dark-state physics. We solve for the steady-state density matrix $\rho_{\rm ss}$ numerically using QuTiP.[50]

According to input-output theory,[27] taking into account the phase accumulation due to waveguide propagation, the transmission coefficient t_{21} (defined as the ratio of the output

field to the input field) can be expressed as a coherent superposition of the radiation fields from the two qubits:[15,27]

$$t_{21} = 1 + \frac{1}{\alpha}\left(\sqrt{\frac{\gamma_1}{2}}\langle a_1\rangle_{\rm ss} + {\rm e}^{-{\rm i}\varphi_{\rm w}}\sqrt{\frac{\gamma_2}{2}}\langle a_2\rangle_{\rm ss}\right). \tag{6}$$

where $\langle a_j\rangle_{\rm ss}$ denotes the expectation value of the annihilation operator for the j-th qubit in the steady state.

Figure 2(a) presents the evolution of the transmission power $|t_{21}|^2$ with respect to the probe frequency $\omega_{\rm p}$ and the modulation amplitude ϵ_Φ. In our numerical simulations, we used typical superconducting circuit parameters: energy relaxation rates $\gamma_1/2\pi = 20$ MHz and $\gamma_2/2\pi = 10$ MHz, pure dephasing rate $\gamma_\phi/2\pi = 0.05$ MHz, coupling strength $g_0/2\pi = 20$ MHz, and phase $\varphi_{\rm w} = \pi/2$.

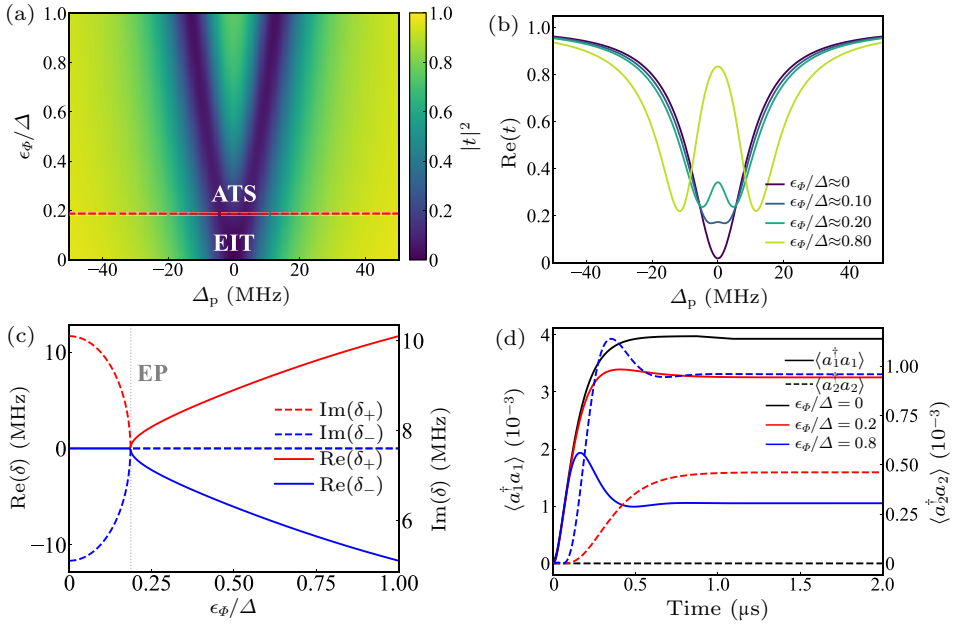


Fig. 2. (a) Two-dimensional map of the power of the transmission $|t_{21}|^2$ as a function of probe frequency $\omega_{\rm p}$ and modulation amplitude ϵ_Φ. The red dashed line indicates the critical boundary of the EIT–ATS transition. (b) Cross-sections of the transmission spectrum at different modulation amplitudes, showing the evolution from a single absorption peak to a doublet splitting. (c) Evolution of the real (solid lines) and imaginary (dashed lines) parts of the complex eigenvalues $\delta_\pm$ with modulation amplitude. The gray dotted line marks the position of the exceptional point (EP), where eigenvalues coalesce and bifurcate. (d) Time evolution dynamics of the excited state populations n_1 and n_2 for qubits 1 and 2.

Since the pure dephasing rate and the anharmonic frequency shifts are much smaller than the energy relaxation rates in the weak-probe regime, we can neglect their effects to derive an analytical understanding. By solving the Lindblad master equation for the steady-state expectations (see Appendix B for a detailed validity discussion including anharmonic corrections), the transmission coefficient can be analytically decomposed into a sum of two Lorentzian functions:[4]

$$t_{21} = 1 + \frac{\chi_+}{\Delta_{\rm p} - \delta_+} + \frac{\chi_-}{\Delta_{\rm p} - \delta_-}, \tag{7}$$

where $\chi_\pm$ represent the effective complex residues associated with the two eigenmodes. The positions of the complex poles are determined by the eigenvalues of the effective non-Hermitian Hamiltonian:

$$\delta_\pm = {\rm i}\frac{\gamma_1+\gamma_2}{4} \pm {\rm i}\sqrt{\Lambda_{\rm eff}^2 + \frac{1}{4}\left(\frac{\gamma_1-\gamma_2}{2}\right)^2}, \tag{8}$$

where we have utilized the linear approximation. It is worth noting that for the specific phase setting $\varphi_{\rm w} = \pi/2$ adopted here, the collective dissipation rate vanishes ($\Gamma_{\rm coll} \propto \cos\varphi_{\rm w} = 0$), implying a purely coherent effective coupling $\Lambda_{\rm eff} \approx {\rm i}\Omega_{\rm eff}$. Based on the sign of the discriminant under the square root, the system's evolution can be rigorously classified into two regimes with distinct physical mechanisms. The boundary between these regimes corresponds to an exceptional point (EP) in non-Hermitian systems.[51,52] When $\Omega_{\rm eff} = |\gamma_1 - \gamma_2|/4$, the discriminant vanishes, and the two eigenvalues $\delta_\pm$ become fully degenerate in the complex plane, marking the emergence of the EP. The red dashed line in Fig. 2(a) clearly delineates this EP trajectory, which constitutes the phase transition boundary from a quantum-interference-dominated (EIT) to a level-splitting-dominated (ATS) regime.[47,53]

Depending on the relative magnitudes of the effective coupling strength $\Omega_{\rm eff}$ and the system dissipation difference $|\gamma_1 - \gamma_2|/4$, the evolution of the transmission spectrum is divided as follows. It is worth noting that since $|\Sigma_{1,2}| \ll \gamma_{1,2}$, the intensity-dependent correction in the discriminant is negligible, allowing the phase transition boundary to be well-approximated by the linear criterion.

First is the weak modulation regime (EIT regime). When the effective coupling is small $\left(\Omega_{\rm eff} < |\gamma_1 - \gamma_2|/4\right)$, the system resides below the EP. As shown in the eigenspectrum

in Fig. 2(c), the real parts of the eigenvalues are degenerate ($\mathrm{Re}(\delta_+) = \mathrm{Re}(\delta_-)$), while their imaginary parts split ($\mathrm{Im}(\delta_+) \neq \mathrm{Im}(\delta_-)$). This indicates the formation of a broad-linewidth bright state and a narrow-linewidth dark state. Physically, this corresponds to the coherent superposition of two Lorentzian lineshapes with opposite signs (one absorption, one gain), resulting in destructive interference. Consequently, the system operates in the quantum interference-dominated (EIT) regime. In this regime, the transmission profile is governed by the subtraction of the broad and narrow linewidths. While a distinct transparency window is not visually resolved under the current parameters, the spectrum maintains a single-peak structure, which is fundamentally distinct from the mode splitting observed in the ATS regime (as shown by the purple and dark blue curves in Fig. 2(b)).

As the modulation amplitude ϵ_Φ increases, the effective coupling strengthens and crosses the EP $\left(\Omega_{\mathrm{eff}} > |\gamma_1 - \gamma_2|/4\right)$, moving the system into the ATS regime. As shown in Fig. 2(c), the imaginary parts of the eigenvalues tend to converge, while the real parts undergo significant Rabi splitting. At this stage, the physical nature of the transmission spectrum transitions to the superposition of two separated absorption peaks (as shown by the light green curve in Fig. 2(b)), signifying ATS.

To further confirm the coherent coupling mechanism established by parametric modulation, Fig. 2(d) displays the time evolution of the qubit excited-state populations. In the absence of modulation ($\epsilon_\Phi = 0$), only the driven qubit 1 occupies the excited state. However, upon introducing modulation, the population of qubit 1 decreases significantly while qubit 2 is effectively excited. This proves that parametric modulation successfully activates a coherent channel controlled by the Bessel function, enabling the system to flexibly switch between EIT and ATS mechanisms.

4. Non-reciprocal transmission via parametric modulation

In conventional waveguide QED systems, where an atom couples to the waveguide at a single point, photon transmission is typically constrained by the Lorentz reciprocity theorem, manifesting as $|t_{21}| = |t_{12}|$. However, in our model, the two spatially separated qubits introduce a non-local propagation phase delay φ_{w}. Combined with the parametric frequency modulation of qubit 2, this configuration incorporates a complex coupling phase factor into the effective Hamiltonian, analogous to those found in giant atom systems.[45,54]

In the previous section, we derived the forward transmission coefficient t_{21}. According to input-output theory, exchanging the input and output ports (i.e., injecting from port 2 and detecting at port 1) reverses the direction of the phase accumulation for photons propagating between the two coupling points (equivalent to $\varphi_{\mathrm{w}} \to -\varphi_{\mathrm{w}}$). Consequently, the backward transmission coefficient t_{12} can be expressed as

$$t_{12} = 1 + \frac{1}{\alpha}\left(\mathrm{e}^{-\mathrm{i}\varphi_{\mathrm{w}}}\sqrt{\frac{\gamma_1}{2}}\langle a_1\rangle_{\mathrm{bw}} + \sqrt{\frac{\gamma_2}{2}}\langle a_2\rangle_{\mathrm{bw}}\right), \tag{9}$$

where $\langle a_i\rangle_{\mathrm{bw}}$ denotes the steady-state expectation value under backward driving.

Comparing the forward and backward transmission, we find that the system exhibits significant non-reciprocity when the waveguide phase $\varphi_{\mathrm{w}} \neq n\pi$. The physical mechanism stems from the interplay between quantum interference and system dissipation. It has been established that breaking the time-reversal symmetry of the Hamiltonian via a phase factor alone is insufficient to induce non-reciprocity in single-photon transmission.[45,55] The simultaneous presence of dissipation channels (provided by $\gamma_{1,2}$ in our system) is essential. These channels ensure that energy traveling along destructively interfering paths cannot reversibly return to the waveguide, thereby creating directional absorption or blocking in the transmission spectrum.[33,45,56,57]

To quantify the non-reciprocal characteristics of the system, we adopt the isolation degree parameter C, defined as[45,55]

$$C = \frac{|t_{21}|^2 - |t_{12}|^2}{|t_{21}|^2 + |t_{12}|^2}. \tag{10}$$

When $C = 0$, the system is reciprocal; when $C \to 1$ or $C \to -1$, the system demonstrates perfect unidirectional transmission properties, behaving like an optical diode.

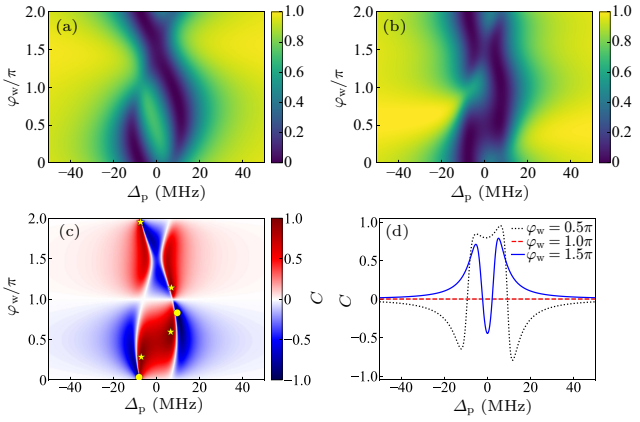


Fig. 3. (a) Map of forward transmittance $|t_{21}|^2$ and (b) backward transmittance $|t_{12}|^2$ as functions of detuning Δ_{p} and phase φ_{w}. (c) The isolation degree C as a function of probe detuning Δ_{p} and waveguide phase φ_{w}. (d) Line cuts of the transmission spectra and isolation degree at the optimal phase. To ensure rigorous accuracy, the data in (c) and (d) were calculated by including the contributions of higher-order harmonics ($n = 0, 1, 2$) beyond the RWA.

We set the system parameters to $\gamma_1/2\pi = 20$ MHz, $\gamma_2/2\pi = 10$ MHz, and $\gamma_\phi/2\pi = 0.05$ MHz. Figures 3(a) and 3(b) display the forward transmittance $|t_{21}|^2$ and backward transmittance $|t_{12}|^2$, respectively, as functions of the probe detuning Δ_{p} and waveguide phase φ_{w}.

The asymmetry in the transmission spectra is immediately apparent. For instance, at specific phases φ_w, a transmission dip (absorption) in the forward direction may correspond to high transmittance in the backward direction. Figure 3(c) illustrates the full distribution of the isolation degree C in the parameter space. The red regions ($C > 0$) and blue regions ($C < 0$) correspond to windows of unidirectional conduction in the forward and backward directions, respectively.

To elucidate the regulatory role of the phase on nonreciprocity, Fig. 3(d) presents slices of C at several typical phases. We observe that when $\varphi_w = n\pi$ (e.g., $\pi, 2\pi$, indicated by the blue dashed line in Fig. 3(d)), the isolation degree becomes identically zero ($C \equiv 0$). This implies that if the waveguide length is exactly an integer multiple of the half-wavelength, the phase difference accumulated by photons round-tripping between the two qubits vanishes. Consequently, the system recovers an effective time-reversal symmetry, exhibiting reciprocal transmission. This behavior is consistent with observations previously reported in giant atom systems.[45]

Conversely, to realize a perfect quantum diode, the nonreciprocity contrast must reach unity ($C = \pm 1$). Theoretically, this ideal limit corresponds to the complete suppression of transmission in one direction (i.e., $t_{12} = 0$ or $t_{21} = 0$), originating from the perfect destructive interference between the coherent and dissipative channels. However, under the current conditions, particularly due to the asymmetry in the radiative decay rates ($\gamma_1 \neq \gamma_2$), the amplitude matching condition required for perfect interference cancellation cannot be strictly satisfied. Consequently, the transmission coefficients cannot completely vanish, preventing the realization of an ideal diode. Nevertheless, the system still exhibits significant non-reciprocal responses close to the diode regime. As visualized in Fig. 3(c), we identify multiple optimal working points where the system exhibits near-perfect non-reciprocity. In the figure, the local maxima and minima are explicitly marked by yellow stars and circles, respectively. Specifically, we observe four maxima and two minima, all satisfying $|C| > 0.98189$. Quantitatively, the four maxima are located at $(\Delta_p/2\pi, \varphi_w/\pi) \approx (6.667\ \text{MHz}, 0.593)$, $(7\ \text{MHz}, 1.14)$, $(-7\ \text{MHz}, 0.283)$, and $(-7.333\ \text{MHz}, 1.95)$, with corresponding isolation degrees of $C \approx 0.99998, 0.99994$, 0.99973, and 0.98189, respectively. The two minima are found at $(9.667\ \text{MHz}, 0.830)$ and $(-8\ \text{MHz}, 0.03)$, with isolation degrees of $C \approx -0.99974$ and -0.99891. The highest isolation performance is achieved at these extrema, demonstrating that the system can function as an approximate quantum diode in either direction by tuning the phase and detuning.

This result has significant experimental implications: although the geometric distance L between the two coupling sites is fixed in a physical device, we can finely tune the phase φ_w by adjusting the frequencies of the two qubits to change the effective wavevector k in the waveguide. This allows for *in situ* switching between reciprocal and non-reciprocal transmission.[55] Experimentally, the feasibility of phase tuning and the system's robustness are determined by the dispersion relation $\mathrm{d}\varphi/\mathrm{d}\omega = L/v$. Since the wave velocity v is constant (determined by the transmission line parameters, typically $v \approx 1.2 \times 10^8$ m/s), the phase sensitivity depends linearly on the inter-qubit distance L. In our design, we restrict L to the range of $\lambda/2$ to λ (e.g., $L = 10$ mm) to suppress susceptibility to noise. Quantitatively, this yields a very small slope of approximately 0.0017π per 10 MHz detuning. This ensures that the system is robust against experimental parameter drifts. Conversely, if higher tunability is required, one can exploit the periodicity of the phase by extending L to the 2π–4π regime (e.g., $L \to 2L$). In this configuration, the slope $\mathrm{d}\varphi/\mathrm{d}\omega$ doubles, allowing for more sensitive "*in situ*" phase tuning via frequency adjustment.

To gain deeper insight into this phenomenon, we derive an analytical expression for the isolation degree C under ideal conditions, neglecting the qubit anharmonicity (implying $\tilde{\Delta}_{1,2} \to \Delta_p$) and pure dephasing ($\gamma_\phi \approx 0$). As derived in detail in Appendix C, following the approach in the relevant literature,[55] the numerator is primarily proportional to the sine of the phase delay:

$$C_{\text{ideal}} = \frac{\sqrt{\gamma_1\gamma_2}\Lambda_{\text{eff}} J_1 \sin\varphi_w}{\mathcal{D}(\Delta_p, \Lambda_{\text{eff}}, \varphi_w)}, \tag{11}$$

where Λ_{eff} represents the effective coupling term and $\mathcal{D}$ is the normalization denominator term (explicitly defined in Eq. (C6) of Appendix C).

This analytical expression clearly elucidates the phenomenon observed in the numerical simulations: the isolation degree must vanish when the condition $\sin(\varphi_w) = 0$ is met. Furthermore, we compared this analytical solution with numerical results incorporating weak dephasing ($\gamma_\phi = 0.05$ MHz), as shown in Fig. 3(c). The high degree of agreement indicates that the non-reciprocal characteristics of this system possess good robustness under physical conditions with weak phase dephasing, effectively resisting environmental noise. Additionally, by varying the modulation amplitude ϵ_Φ, the non-reciprocal response can be dynamically tuned across the frequency spectrum.

5. Directional photon emission via parametric modulation

To evaluate the performance of the system as a tunable quantum emitter, we investigate the spontaneous emission dynamics starting from an initial excited state. Under

the rotating-wave approximation (RWA), the open quantum dynamics of the system is governed by the Lindblad master equation. The effective Hamiltonian H_{emission}, incorporating parametric modulation, is given by

$$H_{\text{emission}} = \omega_1 a_1^\dagger a_1 + \omega_2 a_2^\dagger a_2 + \left(\frac{\sqrt{\gamma_1\gamma_2}}{2}\sin\varphi_{\text{w}} + g_0\right) J_1\left(\frac{\epsilon_\Phi}{\Delta}\right)(a_1^\dagger a_2 + a_1 a_2^\dagger), \tag{12}$$

where we have transformed into a rotating frame referenced to the frequency ω_1 of qubit 1. Here, the effective coupling strength is renormalized by the first-order Bessel function J_1, reflecting the modulation-induced interaction.

To quantify the photon flux propagating to the left (L) and right (R), we employ input–output theory.[27,46] Following the standard waveguide QED formalism, the output field operators $\hat{a}_{\text{L}}$ and $\hat{a}_{\text{R}}$ at the two ends of the waveguide are related to the system operators as

$$\hat{a}_{\text{R}} = \sqrt{\frac{\gamma_1}{2}}a_1 + \mathrm{e}^{-\mathrm{i}\varphi_{\text{w}}}\sqrt{\frac{\gamma_2}{2}}a_2, \tag{13}$$

$$\hat{a}_{\text{L}} = \mathrm{e}^{-\mathrm{i}\varphi_{\text{w}}}\sqrt{\frac{\gamma_1}{2}}a_1 + \sqrt{\frac{\gamma_2}{2}}a_2. \tag{14}$$

Here, the phase factor $\varphi_{\text{w}} = k|x_1 - x_2|$ depends on the inter-qubit distance and the propagation direction of the photons.[48] Consequently, the instantaneous photon flux emitted to the left and right is defined as $n_{\text{L/R}}(t) = \langle \hat{a}^\dagger_{\text{L/R}}(t)\hat{a}_{\text{L/R}}(t)\rangle$.

In our numerical simulations, we first consider the scenario where the system is initialized in the state $|e,g\rangle$, corresponding to the first qubit being excited and the second in the ground state. To clearly demonstrate that the physical mechanism of directional emission originates from frequency modulation, we utilize the parameters $\gamma_1/2\pi = \gamma_2/2\pi = 10$ MHz. Figure 4 illustrates the radiation characteristics under different modulation parameters ϵ_Φ/Δ. Figures 4(a) and 4(b) depict the time evolution of the output flux to the left (n_{L}) and right (n_{R}), respectively, for the initial state $|e,g\rangle$. To demonstrate the ultimate directional capability of the system, Figs. 4(c) and 4(d) show the emission dynamics when the system is initialized in the ideal chiral Bell states.

We first consider the case without frequency modulation ($\epsilon_\Phi/\Delta = 0$, indicated by the black solid lines). Due to the large detuning between the two qubits ($\Delta \gg g$), qubit 2 barely participates in the dynamics. In this regime, the system is physically equivalent to a single excited qubit (qubit 1) coupled to the waveguide. Since the coupling of a single dipole to a 1D waveguide is isotropic,[14] the probability amplitudes for qubit 1 to emit photons to the left and right are identical. Consequently, we observe that the curves for $n_{\text{L}}(t)$ and $n_{\text{R}}(t)$ coincide, and the emitted photon flux in both directions is equal. This confirms that without modulation to break the symmetry, the system exhibits no selective emission.

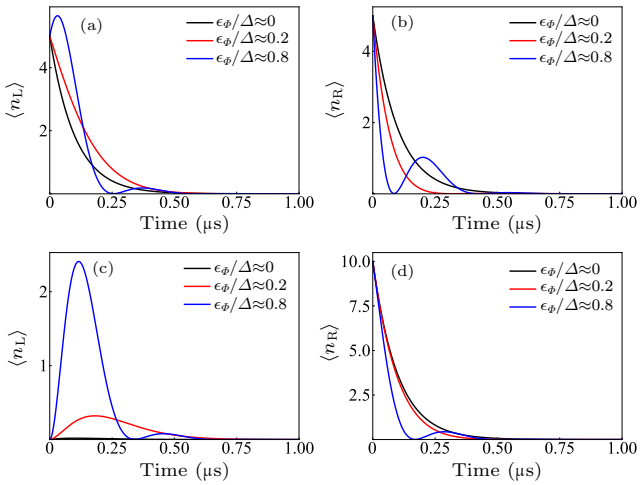


Fig. 4. Selective photon emission dynamics under frequency modulation. (a) Output photon flux to the left, $n_{\text{L}}(t)$, and (b) to the right, $n_{\text{R}}(t)$, when the system is initialized in the product state $|e,g\rangle$. (c) Output photon flux to the left, $n_{\text{L}}(t)$, and (d) to the right, $n_{\text{R}}(t)$, when the system is initialized in the ideal Bell state $|\psi_+\rangle$. The black, red, and blue curves correspond to modulation parameters $\epsilon_\Phi/\Delta = 0$, 0.2, and 0.8, respectively. While the product state yields highly asymmetric emission, the Bell state demonstrates near-unity perfect directionality with suppressed leakage.

When parametric modulation is introduced ($\epsilon_\Phi/\Delta = 0.2, 0.8$, shown by red and blue lines), the radiation symmetry of the system is broken. As evident from Figs. 4(a) and 4(b), the photon flux flowing to the left is significantly higher than that flowing to the right ($n_{\text{L}}(t) > n_{\text{R}}(t)$), demonstrating distinct selective emission characteristics.

The physical mechanism underlying this phenomenon is the waveguide-mediated quantum interference effect, often referred to as the chiral waveguide effect.[48,58] Although the individual coupling parameters of the two qubits to the waveguide are identical, the parametric modulation establishes an effective coherent channel between qubit 1 and qubit 2. The radiation field results from the coherent superposition of fields from two spatially separated emitters. For the left-propagating mode, the matching of the waveguide propagation phase with the relative phase between qubits leads to constructive interference. Conversely, for the right-propagating mode, the channels undergo destructive interference.

This interference results in a preferential emission of photons towards the left port. Notably, this selectivity can be reversed by equivalently altering the phase delay φ_{w} between the two points (e.g., by changing the inter-qubit distance or tuning the center frequency[46]), thereby achieving control over the emission direction.

Although highly asymmetric directional emission is achieved with the initial state $|e,g\rangle$, the leakage to the right is not completely suppressed. The fundamental reason for this imperfect directionality is that the product state $|e,g\rangle$

is inherently a superposition of the ideal chiral Bell states $|\psi_\pm\rangle = (|e,g\rangle \pm \mathrm{i}|g,e\rangle)/\sqrt{2}$.[46,48] To explicitly demonstrate the capability of our system for perfect directional emission, we investigate the output dynamics initialized in the ideal chiral state $|\psi_+\rangle$. As illustrated in Figs. 4(c) and 4(d), the time evolution exhibits near-unity directionality. When the system is initialized in $|\psi_+\rangle$, the emission is perfectly directed to the left channel [Fig. 4(c)], while the photon leakage to the right channel is almost completely suppressed [Fig. 4(d)].

From an experimental perspective, preparing such entangled states prior to emission is highly feasible within current superconducting quantum hardware using a modular architecture.[48] Specifically, the required Bell state can be deterministically generated on "data qubits" that are decoupled from the waveguide, using standard high-fidelity gates. Subsequently, an iSWAP operation, mediated by tunable couplers, can transfer this entangled state directly to the "emitter qubits" on demand. Furthermore, even without the pre-entanglement overhead, initializing the system in the simple product state $|e,g\rangle$ (via a local π-pulse) still yields a prominently asymmetric photon emission. It is anticipated that such an asymmetric emission scheme could potentially be utilized to distinguish different output photon numbers in practical quantum networks equipped with photon-number-resolving detectors.

6. Conclusion

In this work, we have proposed a non-local waveguide QED system based on frequency modulation. By applying parametric modulation to spatially separated and largely detuned superconducting qubits, we successfully constructed an effective Λ-type three-level structure. Our numerical results demonstrate that this system not only realizes the spectral evolution from EIT to ATS but, more crucially, breaks reciprocity by exploiting the non-local phase factor φ_w introduced by waveguide propagation. Unlike local EIT schemes, this approach achieves significant non-reciprocal microwave transmission and direction-selective photon emission. This scheme eliminates the reliance on difficult-to-integrate magnetic components or complex energy-level engineering, operating solely through parametric modulation compatible with standard superconducting circuit fabrication processes. This concise and efficient architecture offers a competitive technological pathway for future on-chip integrated quantum routers, isolators, and microwave photon switches.

Appendix A: Derivation of the effective Hamiltonian under rotating-wave approximation

This appendix provides a detailed derivation of the effective Hamiltonian and the corresponding master equation used in the main text. Our starting point is a system of two atoms with different frequencies, coupled to a one-dimensional waveguide at positions x_1 and x_2. In the laboratory frame, considering the coupling between the atoms and the waveguide continuum, and applying the Born–Markov approximation to eliminate the waveguide degrees of freedom, the non-Hermitian Hamiltonian of the system can be written as[37,49]

$$\begin{aligned} H_{\mathrm{lab}'} &= \omega_1 a_1^\dagger a_1 + \omega_2 a_2^\dagger a_2 \\ &\quad + \alpha_0 a_1^\dagger a_1^\dagger a_1 a_1 + \alpha_0 a_2^\dagger a_2^\dagger a_2 a_2 \\ &\quad - \mathrm{i}\frac{\sqrt{\gamma_1\gamma_2}}{4}\left(\mathrm{e}^{\mathrm{i}k(\omega_1)L} a_1^\dagger a_2 - \mathrm{e}^{-\mathrm{i}k(\omega_1)L} a_1 a_2^\dagger\right) \\ &\quad - \mathrm{i}\frac{\sqrt{\gamma_1\gamma_2}}{4}\left(\mathrm{e}^{\mathrm{i}k(\omega_2)L} a_1 a_2^\dagger - \mathrm{e}^{-\mathrm{i}k(\omega_2)L} a_1^\dagger a_2\right) \\ &\quad + g_0\left(a_1^\dagger a_2 + a_1 a_2^\dagger\right) \\ &\quad - \mathrm{i}\sqrt{\frac{\gamma_1}{2}}\left(\alpha\,\mathrm{e}^{\mathrm{i}(\omega_\mathrm{p}t+\varphi_1)} a_1^\dagger - \alpha^*\,\mathrm{e}^{-\mathrm{i}(\omega_\mathrm{p}t+\varphi_1)} a_1\right) \\ &\quad - \mathrm{i}\sqrt{\frac{\gamma_2}{2}}\left(\alpha\,\mathrm{e}^{\mathrm{i}(\omega_\mathrm{p}t+\varphi_2)} a_2^\dagger - \alpha^*\,\mathrm{e}^{-\mathrm{i}(\omega_\mathrm{p}t+\varphi_2)} a_2\right), \end{aligned} \tag{A1}$$

where $L = |x_1 - x_2|$ is the distance between the two atoms, v is the speed of light in the waveguide, and $k(\omega) = \omega/v$ is the wave number. The parameter α_0 represents the anharmonicity of the two qubits, which we assume to be identical; experimentally, this can be realized by controlling the capacitance of the transmon qubits. The parameter g_0 denotes the direct interaction (e.g., capacitive coupling) between the two atoms. $\gamma_{1,2}$ are the spontaneous emission rates of the two atoms, and α represents the amplitude of the probe field. The phase factors $\varphi_{1,2}$ depend on the direction and position of the incident probe field.

In our experimental setup, the parameters are set as follows: $\omega_1/2\pi = 6$ GHz, $\omega_2/2\pi = 5.8$ GHz, and the probe frequency $\omega_\mathrm{p}/2\pi \approx 6$ GHz. The detuning between the two qubits, $\Delta_{12}/2\pi = 200$ MHz, is much larger than the coupling strengths and decay rates ($\Delta_{12} \gg g, \gamma_1, \gamma_2$), placing the system in the large-detuning regime. Furthermore, we have $g_0/2\pi = 20$ MHz, $\gamma_1/2\pi = 20$ MHz, and $\gamma_2/2\pi = 10$ MHz. Under these conditions, the approximation $\sqrt{\omega_1/\omega_2} \approx 1$ is well justified. More importantly, when we set $\omega_1 L/v = \pi/4$, the corresponding phase factor for the second qubit is $\omega_2 L/v \approx 0.966 \times (\pi/4) \approx \pi/4$, due to the relative proximity of ω_2 to ω_1. Therefore, we can neglect the variation in the phase factor caused by the frequency difference and denote it uniformly as φ_w.

Under these approximations, the Hamiltonian in Eq. (A1) simplifies to Hamiltonian (1):

$$\begin{aligned} H_\mathrm{lab} &= \omega_1 a_1^\dagger a_1 + [\omega_2 + \epsilon_\Phi \cos(\Delta t)]\, a_2^\dagger a_2 \\ &\quad + \alpha_0 a_1^\dagger a_1^\dagger a_1 a_1 + \alpha_0 a_2^\dagger a_2^\dagger a_2 a_2 \end{aligned}$$

$$+\left(g_0+\frac{\sqrt{\gamma_1\gamma_2}}{2}\sin\varphi_{\rm w}\right)(a_1^\dagger a_2+a_1 a_2^\dagger)$$
$$-\mathrm{i}\sum_{j=1,2}\sqrt{\frac{\gamma_j}{2}}\left[(\alpha\,\mathrm{e}^{\mathrm{i}(\omega_{\rm p}t+\varphi_j)}a_j^\dagger-\alpha^*\,\mathrm{e}^{-\mathrm{i}(\omega_{\rm p}t+\varphi_j)}a_j\right]. \tag{A2}$$

To realize controllable coherent coupling, we apply a longitudinal parametric modulation to qubit 2 in the experiment, i.e., $\omega_2(t)=\omega_2+\epsilon_\Phi\cos(\Delta t)$, where Δ is the modulation frequency. To treat this time-dependent term, we move to the interaction picture. Through the unitary transformation $U_1(t)=\exp\left[\mathrm{i}\omega_1 t a_1^\dagger a_1+\mathrm{i}(\omega_2 t+\frac{\epsilon_\Phi}{\Delta}\sin(\Delta t))a_2^\dagger a_2\right]$, the coupling term between the qubits transforms as

$$\tilde{H}_{\rm int}=\tilde{g}\left(a_1^\dagger a_2\,\mathrm{e}^{\mathrm{i}(\omega_1-\omega_2)t+\mathrm{i}\frac{\epsilon_\Phi}{\Delta}\sin(\Delta t)}+\mathrm{H.c.}\right), \tag{A3}$$

where the effective static coupling strength is $\tilde{g}=g_0+\frac{\sqrt{\gamma_1\gamma_2}}{2}\sin\varphi_{\rm w}$. Using the Jacobi–Anger expansion $\mathrm{e}^{-\mathrm{i}z\sin(\theta)}=\sum_{n=-\infty}^{\infty}J_n(z)\,\mathrm{e}^{-\mathrm{i}n\theta}$, we expand the coupling term into a series of harmonic components.

It is important to note that the anharmonic terms $\alpha_0 a_j^\dagger a_j^\dagger a_j a_j$ remain invariant under this unitary transformation. Since $U_1(t)$ is diagonal in the photon number basis (constructed purely from number operators $n_j=a_j^\dagger a_j$), it commutes with the anharmonic terms, i.e., $[U_1(t),a_j^\dagger a_j^\dagger a_j a_j]=0$. Consequently, the form of the nonlinearity is preserved in the interaction picture.

When the modulation frequency satisfies the resonance condition $\Delta=\omega_1-\omega_2$, the $n=1$ term in the expansion ($\mathrm{e}^{-\mathrm{i}\Delta t}$) cancels with the $\mathrm{e}^{\mathrm{i}(\omega_1-\omega_2)t}$ term, generating a time-independent resonant coupling term. Under the rotating-wave approximation (RWA), neglecting other fast-oscillating terms ($n\neq 1$), we obtain the interaction Hamiltonian

$$H_{1,\rm int}=\tilde{g}J_1\left(\frac{\epsilon_\Phi}{\Delta}\right)(a_1^\dagger a_2+\mathrm{H.c.}). \tag{A4}$$

This is consistent with the interaction term in Eq. (2) of the main text. This result demonstrates that by adjusting the modulation amplitude ϵ_Φ, we can precisely control the effective coupling strength $\Omega_{\rm eff}$ via the first-order Bessel function J_1.

Regarding the drive term, a similar Bessel function modulation factor would appear for qubit 2 after the transformation. However, since the probe light is mainly near ω_1 and Δ is large ($\Delta\gg\gamma_{1,2}$), direct driving of qubit 2 is highly detuned. Therefore, in the effective model, the primary physical processes are the inter-qubit coupling controlled by J_1 and the collective dissipation determined by the waveguide phase $\varphi_{\rm w}$.

Including the drive terms, the intermediate Hamiltonian in the interaction picture (before the final frame transformation) can be expressed as

$$H_1=\alpha_0 a_1^\dagger a_1^\dagger a_1 a_1+\alpha_0 a_2^\dagger a_2^\dagger a_2 a_2$$
$$-\mathrm{i}\sqrt{\frac{\gamma_1}{2}}\left[\alpha\,\mathrm{e}^{-\mathrm{i}(\Delta_{\rm p}t+\varphi_1)}a_1^\dagger-\alpha^*\,\mathrm{e}^{\mathrm{i}(\Delta_{\rm p}t+\varphi_1)}a_1\right]$$
$$-\mathrm{i}\sqrt{\frac{\gamma_2}{2}}J_1\left(\frac{\epsilon_\Phi}{\Delta}\right)\left[\alpha\,\mathrm{e}^{-\mathrm{i}(\Delta_{\rm p}t+\varphi_2)}a_2^\dagger-\alpha^*\,\mathrm{e}^{\mathrm{i}(\Delta_{\rm p}t+\varphi_2)}a_2\right]$$
$$+\tilde{g}J_1\left(\frac{\epsilon_\Phi}{\Delta}\right)(a_1^\dagger a_2+a_1 a_2^\dagger), \tag{A5}$$

where $\Delta_{\rm p}=\omega_1-\omega_{\rm p}$ is the probe detuning.

Finally, to eliminate the remaining time dependence in the drive terms and obtain a stationary Hamiltonian, we apply a final unitary transformation $U_2(t)=\exp[-\mathrm{i}\Delta_{\rm p}t(a_1^\dagger a_1+a_2^\dagger a_2)]$. This transforms the system into a frame rotating at the probe frequency $\omega_{\rm p}$. The resulting time-independent effective Hamiltonian matches Eq. (2) in the main text.

Consequently, the open quantum dynamics of the system is governed by the Lindblad master equation

$$\dot{\rho}=-\mathrm{i}[H_{\rm eff},\rho]+\sum_{j=1,2}\mathcal{L}_j[\rho]+\mathcal{L}_{\rm coll}[\rho], \tag{A6}$$

where the collective dissipation term $\mathcal{L}_{\rm coll}[\rho]$ is also influenced by the modulation and the waveguide phase. However, under the RWA and large-detuning conditions, its main contribution comes from the imaginary part of the waveguide-mediated interaction, which contributes to collective decay. For the resonant modulation case of interest, the form of collective dissipation is determined by $\cos\varphi_{\rm w}$, as described in the main text.

The validity of this effective model essentially depends on the spectral separation of the modulation sidebands.[44] In our system, the modulation frequency is set to $\Delta/2\pi=200$ MHz to bridge the detuning between the qubits. In contrast, the maximum effective coupling strength is $\Omega_{\rm eff}/2\pi\approx 12$ MHz. This establishes a clear hierarchy of energy scales: $\Delta\gg\Omega_{\rm eff}$. Consequently, the undesired counter-rotating terms and higher-order harmonics ($n\neq 1$) correspond to transitions that are detuned by at least Δ. Since the coupling strength is significantly smaller than this detuning, these non-resonant processes are energetically suppressed and primarily induce a dispersive renormalization of the qubit frequencies. To rigorously capture these effects, the numerical results presented in Fig. 3 of the main text were calculated by explicitly including the carrier ($n=0$) and second-order ($n=2$) harmonics in addition to the resonant ($n=1$) term. As shown in Fig. 3, while the inclusion of these higher-order terms leads to a slight shift in the resonance frequency due to the strong modulation, the interference-based non-reciprocity mechanism remains robust. The high isolation degree ($C\approx 0.99$) is fully preserved at the shifted resonance frequency, confirming that the system physics is well-described by the effective model with renormalized parameters.

Appendix B: Validity of the linear approximation under mean-field analysis

While the derivation in Appendix A assumes linear harmonic oscillators, realistic superconducting transmon qubits possess inherent anharmonicity. Here, we justify the validity of the linear approximation used in the main text by analyzing the system dynamics with the nonlinear terms under the mean-field approximation.

Incorporating the finite anharmonicity α_0, the effective Hamiltonian is modified to include the Kerr nonlinearity terms: $H_{\rm nl} = \sum_{j=1,2} \alpha_0 a_j^\dagger a_j^\dagger a_j a_j$. Based on the master equation, the evolution of the expectation values of the annihilation operators can be obtained. By applying the mean-field approximation $\langle a_j^\dagger a_j a_j\rangle \approx |a_j|^2\langle a_j\rangle$, we derive the coupled nonlinear equations of motion:

$$\begin{aligned}\dot{a}_1 &= -\mathrm{i}\left(\tilde{\Delta}_1 - \mathrm{i}\left(\frac{\gamma_1}{2}+\gamma_{\phi,1}\right)\right)a_1 - \Lambda_{\rm eff}a_2 + \sqrt{\frac{\gamma_1}{2}}a_{\rm in},\\ \dot{a}_2 &= -\mathrm{i}\left(\tilde{\Delta}_2 - \mathrm{i}\left(\frac{\gamma_2}{2}+\gamma_{\phi,2}\right)\right)a_2 - \Lambda_{\rm eff}a_1\\ &\quad + \sqrt{\frac{\gamma_2}{2}}\,\mathrm{e}^{\mathrm{i}\varphi_{\rm w}}J_1 a_{\rm in},\end{aligned} \tag{B1}$$

where $\Lambda_{\rm eff} = \mathrm{i}\Omega_{\rm eff} + \Gamma_{\rm coll}$. Crucially, the anharmonicity introduces an intensity-dependent detuning shift:

$$\tilde{\Delta}_j = \Delta_{\rm p} + 2\alpha_0|a_j|^2. \tag{B2}$$

This term represents the ac-Stark shift induced by the self-Kerr nonlinearity. The validity of the linear model depends on whether this frequency shift is comparable to the system's characteristic linewidth. In our scheme, the system operates in the weak-probe regime. As shown in the population dynamics in Fig. 2(d) of the main text, under resonant driving conditions, the steady-state average photon number in the first qubit is extremely low, satisfying $\langle n_1\rangle_{\rm ss} = |\alpha_1|^2 \approx 4\times10^{-3}$. Assuming a typical transmon anharmonicity of $\alpha_0/2\pi \approx -180$ MHz, the maximum induced frequency shift is estimated as

$$\begin{aligned}|\delta\omega| = |2\alpha_0\langle n_1\rangle_{\rm ss}| &\approx 2\times 180\ \text{MHz}\times(4\times10^{-3})\\ &\approx 1.44\ \text{MHz}.\end{aligned} \tag{B3}$$

This shift is more than an order of magnitude smaller than the qubit relaxation rate ($\gamma_1/2\pi = 20$ MHz) and the effective coupling strength. Consequently, the nonlinear detuning is negligible.

To explicitly verify the impact of these nonlinear terms on the spectral features, we solve Eq. (B1) for the steady state ($\dot{a}_1 = \dot{a}_2 = 0$). The steady-state expectation values $a_{1,\rm ss}$ and $a_{2,\rm ss}$ can be expressed as

$$\langle a_1\rangle_{\rm ss} = \frac{\sqrt{\frac{\gamma_1}{2}}a_{\rm in}(\mathrm{i}\tilde{\Delta}_2 + \frac{\gamma_2}{2} + \gamma_{\phi_2}) - \sqrt{\frac{\gamma_2}{2}}\,\mathrm{e}^{\mathrm{i}\varphi_{\rm w}}J_1 a_{\rm in}\Lambda_{\rm eff}}{\mathcal{D}(\boldsymbol{n})},$$

$$\langle a_2\rangle_{\rm ss} = \frac{\sqrt{\frac{\gamma_2}{2}}\,\mathrm{e}^{\mathrm{i}\varphi_{\rm w}}\tilde{a}_{\rm in}(\mathrm{i}\tilde{\Delta}_1 + \frac{\gamma_1}{2} + \gamma_{\phi_1}) - \sqrt{\frac{\gamma_1}{2}}a_{\rm in}\Lambda_{\rm eff}}{\mathcal{D}(\boldsymbol{n})}, \tag{B4}$$

where the denominator $\mathcal{D}(\boldsymbol{n})$ is the determinant of the coefficient matrix, which now depends on the photon numbers $\boldsymbol{n} = (|a_1|^2, |a_2|^2)$:

$$\mathcal{D}(\boldsymbol{n}) = \left(\mathrm{i}\tilde{\Delta}_1 + \frac{\gamma_1}{2} + \gamma_{\phi,1}\right)\left(\mathrm{i}\tilde{\Delta}_2 + \frac{\gamma_2}{2} + \gamma_{\phi,2}\right) - \Lambda_{\rm eff}^2. \tag{B5}$$

By finding the roots of $\mathcal{D}(\boldsymbol{n}) = 0$, we derive the modified eigenvalues of the non-Hermitian Hamiltonian. This leads to the intensity-dependent correction to Eq. (8) (where collective dissipation was neglected):

$$\begin{aligned}\tilde{\delta}_\pm = \mathrm{i}&\left(\frac{\gamma_1+\gamma_2}{4} + \bar{\gamma}_\phi\right) - \bar{\Sigma}\\ &\pm \sqrt{\Lambda_{\rm eff}^2 + \left[\frac{\gamma_1-\gamma_2}{4} + \Delta\gamma_\phi + \mathrm{i}\Delta\Sigma\right]^2},\end{aligned} \tag{B6}$$

where $\bar{\gamma}_\phi = (\gamma_{\phi,1}+\gamma_{\phi,2})/2$ and $\Delta\gamma_\phi = (\gamma_{\phi,1}-\gamma_{\phi,2})/2$ are the average and differential pure dephasing rates. The terms $\bar{\Sigma} = (\Sigma_1+\Sigma_2)/2$ and $\Delta\Sigma = (\Sigma_1-\Sigma_2)/2$ correspond to the total and relative frequency shifts induced by the anharmonicity $\Sigma_j = 2\alpha_0|a_j|^2$. A comparison with the linear eigenvalues $\delta_\pm$ reveals that anharmonicity induces a global frequency shift and modifies the mode splitting via the effective detuning mismatch $\Delta\Sigma$.

It is particularly important to assess the impact of asymmetric dephasing on the spectral line shape. As indicated by the discriminant in Eq. (B6), the spectral evolution is governed by the total dissipation difference $[(\gamma_1-\gamma_2)/2 + \Delta\gamma_\phi]$. In our experimental regime, the radiative decay mismatch dominates, with $(\gamma_1-\gamma_2)/2 = 5$ MHz. Even under strong modulation where the second qubit's dephasing increases significantly (e.g., $\gamma_{\phi,2}/2\pi \approx 1.5$ MHz) while the first remains static ($\gamma_{\phi,1}/2\pi \approx 0.1$ MHz), the differential dephasing term $\Delta\gamma_\phi \approx -0.7$ MHz acts only as a minor perturbation. It reduces the effective dissipation gap but does not close it. Consequently, the distinct imaginary parts of the eigenvalues are preserved, ensuring that the transparency window remains robust against modulation-induced dephasing.

Consequently, the transmission coefficient t_{21} defined in Eq. (6) evolves into the modified form

$$t_{21} = 1 + \frac{\tilde{\chi}_+}{\tilde{\Delta}_1 - \tilde{\delta}_+} + \frac{\tilde{\chi}_-}{\tilde{\Delta}_2 - \tilde{\delta}_-}. \tag{B7}$$

However, given the estimation $\Sigma_{1,2} \ll \gamma_{1,2}$ derived above, we have $\tilde{\delta}_\pm \approx \delta_\pm$, and Eq. (B7) effectively reduces to the linear Lorentzian form presented in the main text.

Appendix C: Derivation of the isolation degree and normalization factor

Having established the validity of the linear approximation in Appendix B, we now derive the analytical expressions for the isolation degree C and the normalization denominator $\mathcal{D}$ appearing in Eq. (11) of the main text. To obtain the concise form shown in Eq. (11), we neglect the qubit anharmonicity (implying $\tilde{\Delta}_{1,2} \to \Delta_{\rm p}$) and pure dephasing ($\gamma_\phi \approx 0$).

By substituting the steady-state qubit expectation values into the input–output boundary condition, the forward and backward transmission coefficients can be compactly expressed as ratios of a numerator function $\mathcal{N}$ and a common system determinant $\mathcal{M}$:

$$t_{21} = \frac{\mathcal{N}_{21}}{\mathcal{M}}, \quad t_{12} = \frac{\mathcal{N}_{12}}{\mathcal{M}}. \tag{C1}$$

Here, the linear system determinant is given by $\mathcal{M} = (\mathrm{i}\Delta_{\rm p} + \frac{\gamma_1}{2})(\mathrm{i}\Delta_{\rm p} + \frac{\gamma_2}{2}) - \Lambda_{\rm eff}^2$. The explicit form of the forward numerator $\mathcal{N}_{21}$ is

$$\mathcal{N}_{21} = \mathcal{M} + \frac{\gamma_1}{2}\left(\mathrm{i}\Delta_{\rm p} + \frac{\gamma_2}{2}\right) + \frac{\gamma_2}{2}J_1\left(\mathrm{i}\Delta_{\rm p} + \frac{\gamma_1}{2}\right)\mathrm{e}^{-\mathrm{i}\varphi_{\rm w}} - \frac{\sqrt{\gamma_1\gamma_2}}{2}\Lambda_{\rm eff}(J_1\,\mathrm{e}^{-\mathrm{i}\varphi_{\rm w}} + 1). \tag{C2}$$

The backward numerator $\mathcal{N}_{12}$ is obtained by the symmetry transformation $\varphi_{\rm w} \to -\varphi_{\rm w}$:

$$\mathcal{N}_{12} = \mathcal{M} + \frac{\gamma_1}{2}\left(\mathrm{i}\Delta_{\rm p} + \frac{\gamma_2}{2}\right) + \frac{\gamma_2}{2}J_1\left(\mathrm{i}\Delta_{\rm p} + \frac{\gamma_1}{2}\right)\mathrm{e}^{\mathrm{i}\varphi_{\rm w}} - \frac{\sqrt{\gamma_1\gamma_2}}{2}\Lambda_{\rm eff}(J_1\,\mathrm{e}^{\mathrm{i}\varphi_{\rm w}} + 1). \tag{C3}$$

Finally, substituting these expressions into the definition of the isolation degree $C = (|t_{21}|^2 - |t_{12}|^2)/(|t_{21}|^2 + |t_{12}|^2)$, we can identify the specific structure of Eq. (11). The isolation degree is expressed as

$$C = \frac{|\mathcal{N}_{21}|^2 - |\mathcal{N}_{12}|^2}{|\mathcal{N}_{21}|^2 + |\mathcal{N}_{12}|^2}. \tag{C4}$$

To bridge this exact expression with the simplified sinusoidal form in the main text, we factorize the numerator term using the difference of squares approximation:

$$|\mathcal{N}_{21}|^2 - |\mathcal{N}_{12}|^2 = (|\mathcal{N}_{21}| + |\mathcal{N}_{12}|) \times (|\mathcal{N}_{21}| - |\mathcal{N}_{12}|) \approx (|\mathcal{N}_{21}| + |\mathcal{N}_{12}|)\sqrt{\gamma_1\gamma_2}\Lambda_{\rm eff}J_1 \sin\varphi_{\rm w}. \tag{C5}$$

Here, the term $\sqrt{\gamma_1\gamma_2}\Lambda_{\rm eff}J_1 \sin\varphi_{\rm w}$ directly corresponds to the sinusoidal numerator presented in Eq. (11). Consequently, the remaining terms are absorbed into the normalization denominator $\mathcal{D}$, which takes the form

$$\mathcal{D}(\Delta_{\rm p}, \Lambda_{\rm eff}, \varphi_{\rm w}) \approx \frac{|\mathcal{N}_{21}|^2 + |\mathcal{N}_{12}|^2}{|\mathcal{N}_{21}| + |\mathcal{N}_{12}|}. \tag{C6}$$

This derivation clarifies that while the non-reciprocity is fundamentally driven by the $\sin\varphi_{\rm w}$ interference, the exact amplitude is modulated by the complex denominator factor $\mathcal{D}$.

Acknowledgements

This work was supported by the National Natural Science Foundation of China (Grant Nos. 12574540, 92265207, and T2121001) and Quantum Science and Technology – National Science and Technology Major Project of China (Grant No. 2021ZD0301800).

References

[1] Blais A, Grimsmo A L, Girvin S M and Wallraff A 2021 *Rev. Mod. Phys.* **93** 025005

[2] Wallraff A, Schuster D I, Blais A, Frunzio L, Huang R S, Majer J, Kumar S, Girvin S M and Schoelkopf R J 2004 *Nature* **431** 162

[3] You J Q and Nori F 2011 *Nature* **474** 589

[4] Gu X, Kockum A F, Miranowicz A, Liu Y X and Nori F 2017 *Physics Reports* **718–719** 1

[5] Krantz P, Kjaergaard M, Yan F, Orlando T P, Gustavsson S and Oliver W D 2019 *Appl. Phys. Rev.* **6** 021318

[6] Arute F, Arya K, Babbush R, *et al.* 2019 *Nature* **574** 505

[7] Koch J, Yu T M, Gambetta J, Houck A A, Schuster D I, Majer J, Blais A, Devoret M H, Girvin S M and Schoelkopf R J 2007 *Phys. Rev. A* **76** 042319

[8] Houck A A, Schuster D I, Gambetta J M, Schreier J A, Johnson B R, Chow J M, Frunzio L, Majer J, Devoret M H, Girvin S M and Schoelkopf R J 2007 *Nature* **449** 328

[9] Bozyigit D, Lang C, Steffen L, Fink J M, Eichler C, Baur M, Bianchetti R, Leek P J, Filipp S, Da Silva M P, Blais A and Wallraff A 2011 *Nat. Phys.* **7** 154

[10] DiCarlo L, Chow J M, Gambetta J M, Bishop L S, Johnson B R, Schuster D I, Majer J, Blais A, Frunzio L, Girvin S M and Schoelkopf R J 2009 *Nature* **460** 240

[11] Gambetta J M, Houck A A and Blais A 2011 *Phys. Rev. Lett.* **106** 030502

[12] Li K and Zhao J L 2024 *Chin. Phys. B* **33** 090306

[13] Inomata K, Lin Z, Koshino K, Oliver W D, Tsai J S, Yamamoto T and Nakamura Y 2016 *Nat. Commun.* **7** 12303

[14] Roy D, Wilson C M and Firstenberg O 2017 *Rev. Mod. Phys.* **89** 021001

[15] Abdumalikov A A, Astafiev O, Zagoskin A M, Pashkin Yu A, Nakamura Y and Tsai J S 2010 *Phys. Rev. Lett.* **104** 193601

[16] Hoi I C, Wilson C M, Johansson G, Palomaki T, Peropadre B and Delsing P 2011 *Phys. Rev. Lett.* **107** 073601

[17] Zhang Y X, I Carceller C R, Kjaergaard M and Sørensen A S 2021 *Phys. Rev. Lett.* **127** 233601

[18] Hu Y, Li S Y, Chen E Q, Zhang J, Liu Y x, Feng J G and Peng Z 2025 *Appl. Phys. Lett.* **128** 154004

[19] Duan L M, Lukin M D, Cirac J I and Zoller P 2001 *Nature* **414** 413

[20] Kimble H J 2008 *Nature* **453** 1023

[21] Hoi I C, Kockum A F, Palomaki T, Stace T M, Fan B, Tornberg L, Sathyamoorthy S R, Johansson G, Delsing P and Wilson C M 2013 *Phys. Rev. Lett.* **111** 053601

[22] Chen W, Beck K M, Bücker R, Gullans M, Lukin M D, Tanji-Suzuki H and Vuletić V 2013 *Science* **341** 768

[23] Novikov S, Sweeney T, Robinson J E, Premaratne S P, Suri B, Wellstood F C and Palmer B S 2016 *Nat. Phys.* **12** 75

[24] Long J, Ku H S, Wu X, Gu X, Lake R E, Bal M, Liu Y X and Pappas D P 2018 *Phys. Rev. Lett.* **120** 083602

[25] Sillanpää M A, Li J, Cicak K, Altomare F, Park J I, Simmonds R W, Paraoanu G S and Hakonen P J 2009 *Phys. Rev. Lett.* **103** 193601

[26] Brehm J D, Gebauer R, Stehli A, Poddubny A N, Sander O, Rotzinger H and Ustinov A V 2022 *Appl. Phys. Lett.* **121** 204001

[27] Lalumière K, Sanders B C, Van Loo A F, Fedorov A, Wallraff A and Blais A 2013 *Phys. Rev. A* **88** 043806

[28] Van Loo A F, Fedorov A, Lalumière K, Sanders B C, Blais A and Wallraff A 2013 *Science* **342** 1494

[29] Chu K I, Liao W T and Chen Y F 2023 *Phys. Rev. Res.* **5** 033192

[30] Chu K I, Lu X C, Chiang K H, Lin Y H, Chen C D, Yu I A, Liao W T and Chen Y F 2025 *Phys. Rev. Res.* **7** L012015

[31] Chiang K H and Chen Y F 2022 *Phys. Rev. A* **106** 023707

[32] Sounas D L and Alù A 2017 *Nat. Photon.* **11** 774

[33] Metelmann A and Clerk A A 2015 *Phys. Rev. X* **5** 021025

[34] Yu Z and Fan S 2009 *Nat. Photon.* **3** 91

[35] Cao X, Irfan A, Mollenhauer M, Singirikonda K and Pfaff W 2024 *Phys. Rev. Appl.* **22** 064023

[36] Yang L P and Chang Y 2024 *Phys. Rev. A* **110** 023722

[37] Nefedkin N, Cotrufo M, Krasnok A and Alù A 2022 *Advanced Quantum Technologies* **5** 2100112

[38] Li H, Zhang X, Zeng R, Hu M, Xu M, Zhou X, Xia X, Xu J and Yang Y 2024 *Opt. Express* **32** 38292

[39] Dai J Y, Zhao M D, Zhou Y and Xin J 2026 *Chin. Phys. B* **35** 027301

[40] Frisk Kockum A 2021 *International Symposium on Mathematics, Quantum Theory, and Cryptography* ed Takagi T, Wakayama M, Tanaka K, Kunihiro N, Kimoto K and Ikematsu Y (Singapore: Springer Singapore) **33** pp. 125–146

[41] Kannan B, Ruckriegel M J, Campbell D L, Frisk Kockum A, Braumüller J, Kim D K, Kjaergaard M, Krantz P, Melville A, Niedzielski B M, Vepsäläinen A, Winik R, Yoder J L, Nori F, Orlando T P, Gustavsson S and Oliver W D 2020 *Nature* **583** 775

[42] Sheremet A S, Petrov M I, Iorsh I V, Poshakinskiy A V and Poddubny A N 2023 *Rev. Mod. Phys.* **95** 015002

[43] Miao Q and Agarwal G S 2025 *Phys. Rev. Res.* **7** 013138

[44] Joshi C, Yang F and Mirhosseini M 2023 *Phys. Rev. X* **13** 021039

[45] Chen Y T, Du L, Guo L, Wang Z, Zhang Y, Li Y and Wu J H 2022 *Commun. Phys.* **5** 215

[46] Kannan B, Campbell D L, Vasconcelos F, Winik R, Kim D K, Kjaergaard M, Krantz P, Melville A, Niedzielski B M, Yoder J L, Orlando T P, Gustavsson S and Oliver W D 2020 *Science Advances* **6** eabb8780

[47] Anisimov P M, Dowling J P and Sanders B C 2011 *Phys. Rev. Lett.* **107** 163604

[48] Kannan B, Almanakly A, Sung Y, Di Paolo A, Rower D A, Braumüller J, Melville A, Niedzielski B M, Karamlou A, Serniak K, Vepsäläinen A, Schwartz M E, Yoder J L, Winik R, Wang J I J, Orlando T P, Gustavsson S, Grover J A and Oliver W D 2023 *Nat. Phys.* **19** 394

[49] Kockum A F, Johansson G and Nori F 2018 *Phys. Rev. Lett.* **120** 140404

[50] Johansson J R, Nation P D and Nori F 2012 *Computer Physics Communications* **183** 1760

[51] Nie W, Shi T, Liu Y X and Nori F 2023 *Phys. Rev. Lett.* **131** 103602

[52] Heiss W D 2012 *J. Phys. A: Math. Theor.* **45** 444016

[53] Liu Q C, Li T F, Luo X Q, Zhao H, Xiong W, Zhang Y S, Chen Z, Liu J S, Chen W, Nori F, Tsai J S and You J Q 2016 *Phys. Rev. A* **93** 053838

[54] Ren Y M, Pan X F, Yao X Y, Huo X W, Zheng J C, Hei X L, Qiao Y F and Li P B 2025 *Phys. Rev. Res.* **7** 023287

[55] Cai G, Lu Y, Ma X S, Cheng M T and Huang X 2023 *Opt. Express* **31** 33015

[56] Gong R Y,He Z Y, Yu C H, Zhang G F, Nori F and Xiang Z L 2024 arXiv: 2411.19307

[57] Zou J P, Gong R Y and Xiang Z L 2022 *Frontiers in Physics* **10** 896827

[58] Lodahl P, Mahmoodian S, Stobbe S, Rauschenbeutel A, Schneeweiss P, Volz J, Pichler H and Zoller P 2017 *Nature* **541** 473